Rapid Polyolefin Plastics Hydrogenolysis Mediated by Single-Site Heterogeneous Electrophilic/Cationic Organo-Group IV Catalysts

Wilson C. Edenfield[a], Alexander H. Mason[a], Qingheng Lai[a], Amol Agarwal[b], Takeshi Kobayashi[c]*, Yosi Kratish[a]*, Tobin J. Marks[a]*

[a]*Department of Chemistry, Northwestern University, 2145 Sheridan Road, Evanston, IL 60208, USA*

[b]*Department of Materials Science & Engineering, Northwestern University, 2220 Campus Drive, Evanston, IL 60208-3113 USA*

[c]*U.S. DOE Ames National Laboratory, Ames, Iowa 50011-3020, United States*

KEYWORDS polyolefin waste, chemical recycling, sulfated alumina, hafnium, zirconium, hydrogenolysis

ABSTRACT: A homologous series of cationic electrophilic group IV metal hydrides (M = Ti, Zr, Hf) created by chemisorption of the corresponding MNp_4 precursors on highly Brønsted acidic sulfated alumina (AlS) to yield loosely coordinated surface AlS/MNp_2 (Np = neopentyl) species are systematically characterized by ICP, EXAFS/XANES, DRIFTS, and solid-state high-resolution multi-dimensional NMR spectroscopy (SSNMR), as well as by energy span DFT computation. With effective stirring, these complexes readily undergo reaction with H_2 to yield AlS/M(alkyl)H species which are highly active for the hydrogenolysis of diverse commercial polyethylenes, α-olefin-ethylene copolymers, isotactic polypropylene, and post-consumer polyolefins including high-density polyethylenes, yielding medium and small linear and branched hydrocarbons at turnover frequencies as high as 36,300 h^{-1} at 200 °C/17 atm H_2 for M = Zr. For a given polyolefin and reaction conditions, turnover frequencies scale approximately as M = Zr > Hf > Ti, while catalyst thermal stability scales approximately as M = Hf ≈ Zr > Ti, and these trends are qualitatively understandable from the DFT analysis. These catalytic results reveal that the AlS/Hf(R)H- mediated hydrogenolysis favors wax-like and liquid products while the AlS/Zr(R)H-mediated hydrogenolysis can be tuned between gases and liquids. DFT analysis identifies β-alkyl elimination as the turnover-limiting C-C scission process, which is particularly facile in these cationic d^0 complexes, but not so in the neutrally charged analogues.

Introduction

Global plastics waste accumulation is a serious and growing challenge. Annual synthetic, petroleum-based plastics production has increased from less than 2 million tons in 1950 to 380 million tons in 2015 and is projected to double again by 2040. Globally, 18% and 24% of non-fiber plastic waste is recycled or incinerated, respectively, and less than 10% is recycled in the United States.[1] Although preferable to accumulation/landfilling, recycling is typically carried out by a mechanical or melt-and-remold process, yielding a product with inferior thermal, optical, and mechanical resilience.[2, 3] Plastics incineration recovers only a fraction of the energy used in the production of the material as heat, and may co-produce toxic combustion byproducts and greenhouse CO_2, making it unacceptable as a "green" process.[4, 5]

Versatile, durable, lightweight, and low-cost polyolefins are produced on a huge scale for economically essential products such as light-weight automotive and machinery parts, PPEs and prosthetics, construction materials, shoes and clothing, products for agriculture, food packaging/storage, solar cell encapsulation, etc. Note that polyethylene (PE) copolymers and homopolymers, classified as low-density (LDPE) or high-density (HDPE), respectively, currently constitute the largest fraction of all plastic waste (36% by mass). They can be depolymerized by pyrolysis at temperatures over 400 °C, in an unselective process that produces low-value mixtures of hydrocarbons and char.[6-8]

Catalytic hydrogenolysis processes have been the subject of increasing interest as a means to convert polyolefin waste into more valuable products.[9-11] Here polyolefin chain scission can be achieved with abundant grey, blue, or green H_2 to produce lighter hydrocarbons, including wax-range materials as a form of upcycling. Most of the catalysts employed are supported precious metal-based Pd, Pt, Ru, or Re catalysts, used at relatively high temperatures, H_2 pressures, and catalyst loadings, reflecting relatively sluggish activity.[11-22] Some of these catalysts can exhibit high selectivity through upcycling of the PE-derived products, but exhibit only limited activity with polypropylene (PP) and branched polyolefin copolymers.[19] Furthermore, while the heterogeneous nature of these catalysts may impart significant thermal stability and recyclability, atomistic characterization of the catalytically active sites among other sites remains challenging, and for these reasons defining the actual reaction mechanism(s) either experimentally or theoretically is similarly challenged.

For all the above reasons, we sought alternative catalytic systems with earth-abundant metals and having better

defined structural characteristics, focusing on single-site heterogeneous catalysts (SSHCs)[23-26] derived from earth-abundant molecular organometallic precursors and supports that function as both weakly bound ligands and electrophilic precatalyst activators.[27, 28] We initially focused on well-defined molecule-derived electrophilic/cationic organozirconium systems supported on sulfated metal oxides, which were known to be highly active SSHCs for olefin polymerization and hydrogenation as well as stereoselective arene hydrogenation (**Figure 1A**).[29-33] This Laboratory recently reported the facile hydrogenolysis of alkanes and polyolefins under mild conditions, catalyzed by the SSHC AlS/Zr(R)H species where R = alkyl, synthesized by the chemisorption of $ZrNp_4$ on sulfated aluminum oxide (AlS) (**Figure 1B**).[27, 28] The high surface area AlS offers highly Brønsted acidic surface -OH groups while the deprotonated conjugate basic counterpart provides weak/weakly coordinating Brønsted basic counteranions.[34, 35] There, we reported very rapid (at that time), non-mass transport limited hydrogenolysis of hexadecane with TOF = 690 h^{-1} at 150 °C/2.5 atm H_2 pressure, and of pristine laboratory-synthesized polyethylene under similar conditions, using a simple magnetically stirred optically transparent glass pressure reactor. The catalyst was characterized by DRIFTS vibrational spectroscopy, 1-D ^1H MAS NMR spectroscopy, Zr EAXFS/XANES, and DFT computation, consistent with an electrophilic cation-like d^0 organozirconium center as depicted in **Figure 1B**. The relatively high hydrogenolysis activity was attributed to the cationic/electrophilic nature of the d^0 metal center, stabilized by the highly Brønsted acidic sulfated alumina, with the turnover-limiting C-C cleavage step proceeding primarily via β-alkyl elimination.[27, 28, 36, 37]

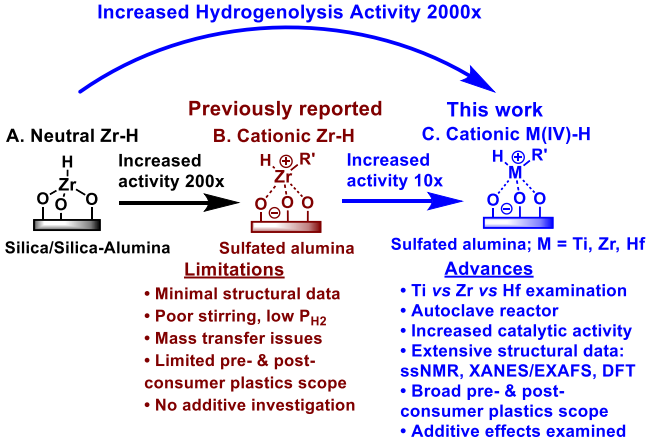

Figure 1. Catalytic properties of single-site heterogeneous organo-group IV catalysts **A**. Neutrally charged Zr hydrocarbyl adsorbate on a weak Brønsted acid surface[29], **B.** $AlS/Zr(alkyl)_2$ -derived cationic adsorbate on a very strong sulfated alumina (AlS) Brønsted acidic surface and their limitations, **C.** Generalized $AlS/M(alkyl)_2$ -derived cationic catalysts on sulfated alumina (AlS; M = Ti, Zr, Hf), and advances reported in this work.

The aforementioned results raise intriguing questions: 1) How does the Zr catalyst perform under more conventional heterogeneous catalytic reactor conditions? Are there changes in activity and selectivity? 2) How general are the Zr catalytic trends vis-à-vis the other group 4 metals? What are the significant differences? 3) Can DFT-level computation account for observed trends in this group 4 series and what are the basis for these trends? 4) How transferable are the present catalytic results to the behavior of various "real world" commercial polyolefins with typical commercial additives? What are the similarities and differences?

Here we report the systematic chemisorption and characterization of the group IV series MR_4 where M = Ti, Hf and R = neopentyl on sulfated alumina (Hammett acidity, H_0 = -14.6)[38] to yield the corresponding SSHCs AlS/MNp_2 which are characterized structurally by EXAFS/XANES, DRIFTS, and 1-D/2-D multinuclear solid-state NMR spectroscopy. It will be seen that that these supported organometallic species yield AlS/M(R)H species (**Figure 1C**) upon treatment with H_2, which catalyze the rapid, solventless hydrogenolysis of polyethylenes, polyethylene-co-1-octenes, and isotactic-polypropylene containing standard commercial additives under very mild conditions. With high speed magnetically coupled stirring in a stainless-steel autoclave reactor, it will be seen that $AlS/ZrNp_2$ catalyzes PE hydrogenolysis with turnover frequencies as high as 36,300 mol (CH_2 units) ·mol $(Zr)^{-1}$·h^{-1} at 200°C/17 atm H_2 pressure with no evidence of significant mass transfer limitations or coking. It will also be seen that the corresponding $AlS/HfNp_2$ and $AlS/TiNp_2$ catalysts mediate polyolefin hydrogenolysis at slightly lower rates than the $AlS/ZrNp_2$ analogue and with the marked catalyst thermal stability trend of Hf, Zr > Ti. Selectivities to various hydrocarbon products are also found to vary significantly with M and the substrate. Hydrogenolysis rates and liquid product selectivity of highly viscous post-consumer products can be increased by the addition of surprisingly inert decalin as a solvent. Furthermore, energy span DFT analysis successfully explains a number of the otherwise counterintuitive but important observations and maps out reaction coordinates in good agreement with experiment.

Below, we first discuss the synthesis and SSNMR, EXAFS, DRIFTS, and DFT characterization of the subject catalysts. Then a comparison of the glass and autoclave reactor results is discussed, followed by, metal center and substrate effects, and solvent effects on HDPE hydrogenolysis. Finally, DFT analysis of the catalytic mechanism is presented, followed by a discussion of polyolefin hydrogenolysis scope and conclusions.

Results

Catalyst Synthesis and Structural Characterization

Chemisorption of MNp_4 on AlS (Full details in the SI)

In a two-sided fritted reaction vessel, dry pentane was condensed onto well-mixed quantities of 0.18 – 0.23 mmol of the corresponding MNp_4 compound and excess (1.000 g) AlS. The resulting slurry was stirred at 25 °C for 1 h, and the resulting solid adsorbate was collected by filtration. The AlS/MNp_2 product was washed repeatedly with dry pentane and dried in vacuo to yield a pale-yellow product for M = Zr, and colorless/white products for M = Ti and Hf. The catalysts were stored in sealed containers at room temperature in an argon glovebox. The catalyst (AlS/MNp_2)

loadings determined by ICP were 0.87 wt. % Ti, 1.40 wt. % Zr, and 3.28 wt. % Hf, respectively.

Catalyst Characterization - Solid-State NMR Spectroscopy

The low-temperature (100 K) ^{1}H MAS NMR spectrum of AlS/HfNp$_2$ reveals a sharp resonance at δ_{1H} 1.1 ppm, assignable to neopentyl ligand alkyl protons, and a broad resonance at δ_{1H} 2.76 ppm assignable to Al-OH moieties (**Figure 2A**).[39, 40] Upon treatment of AlS/HfNp$_2$ with H$_2$, the intensity of the alkyl signal at δ_{1H} 1.12 ppm falls appreciably and most notably, while a new signal grows in at δ_{1H} 19.20 ppm. The latter signal is assignable to a Hf-H species, in agreement with a previously reported Hf hydride supported on silica.[41] Note that these results parallel previous solid-state NMR measurments of AlS/ZrNp$_2$ and AlS/ZrRH, with the Zr-H occurring at δ_{1H} 11. ppm.[27, 28] The ^{13}C{^{1}H} CP-MAS NMR spectrum of AlS/HfNp$_2$ (99% ^{13}C- labeled at the neopentyl CH$_2$) reveals further information, exhibiting signals at δ_{13C} 99.6, 82.9, 54.0, and 26.3 ppm (**Figure 2B**, black line). Assignment of the signal at δ_{13C} 99.6 ppm is straightforwardly made by noting its near-absence in the ^{13}C spectrum of AlS/HfRH **(Figure 2B,** red line); thus, it is assigned to a Hf-CH$_2$ group. While the δ_{13C} 99.6 ppm signal is largely absent from the ^{13}C CPMAS spectrum after H$_2$ treatment, all other signals retain similar intensities, implying that species responsible for the signals at δ_{13C} 82.9, 54.0, and 26.3 ppm are less reactive towards H$_2$ than the Hf-alkyl species. A sharp signal at δ_{13C} 82.9 ppm is likely an aluminum alkoxy species, given its minimal change in intensity on H$_2$ treatment and literature assignments of the ^{13}C chemical shift of similar species.[42] The signal at δ_{13C} 54.0 ppm was not assigned and is likely an unidentified alkoxy species. The signal at δ_{13C} 26.3 ppm is assigned to an Al-CH$_2$ moiety formed upon chemisorption of HfNp$_4$ on AlS. A similar signal was observed previously for AlS/ZrNp2 and is likely attributable to a similar species.[2728]

The ^{13}C{^{1}H} frequency-switched Lee-Goldburg Heteronuclear Correlation (FSLG-HETCOR) spectrum[43-45] provides further support for both ^{1}H and ^{13}C assignments (**Figure 2C**). The signal at δ_{13C} 99.6 ppm displays a cross-peak in the ^{1}H dimension at δ_{1H} 0.8 ppm (note that the ^{1}H chemical shifts change significantly at room temperature *vs.* 100K, see **Figure S1**). The signal at δ_{13C} 82.9 ppm correlates with a signal at δ_{1H} 3.8 ppm and is assigned to Al-O-CH$_2$- carbons. This shift in the ^{1}H dimension agrees well with literature reports of similar moieties.[46] The signal at δ 23.6 ppm is assigned to Al-CH$_2$- moieties and correlates with a signal at δ_{1H} 0.4 ppm, also in agreement with literature assignments of supported aluminum alkyls.[47] To further bolster these assignments, rotational echo saturation pulse double

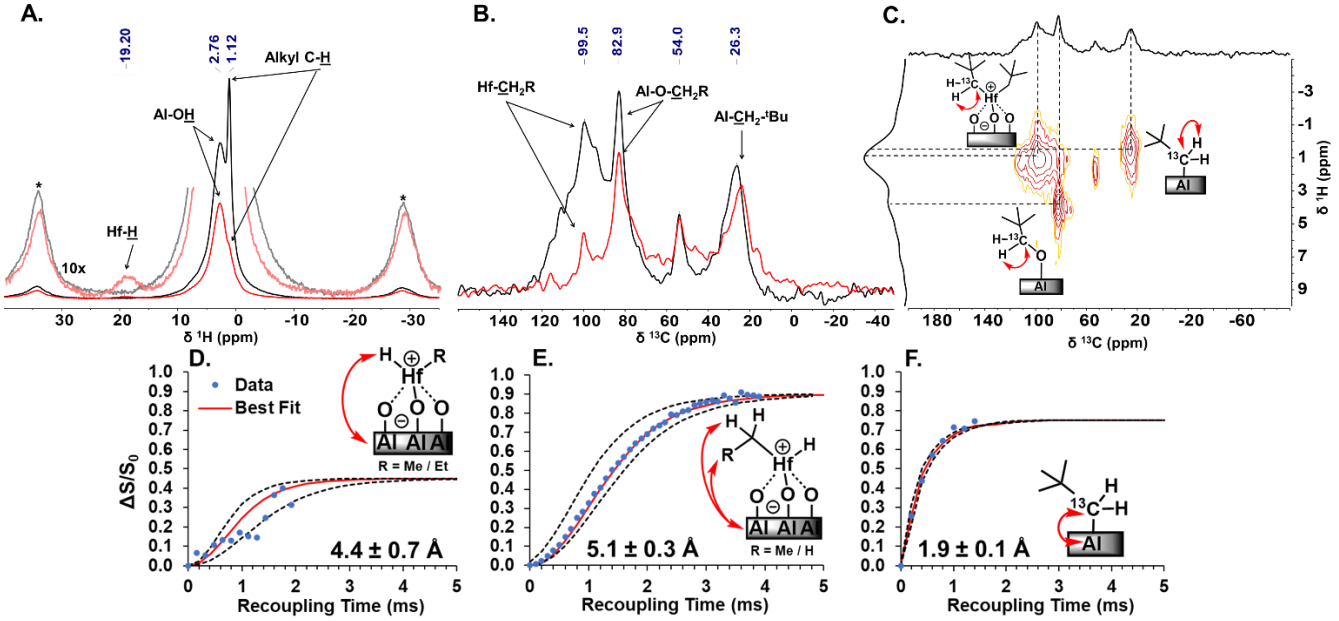

Figure 2. **A** ^{1}H Hahn-echo NMR spectra of AlS/HfNp$_2$ (black) and AlS/Hf(R)H (red), Overlay: 10x zoom, 100 K, 12.5 kHz MAS, 80 μs echo delay, 3s recycle delay, 64 scans, 3.2 mm sapphire rotor, 400 MHz ^{1}H. (*spinning sidebands) **B**. ^{13}C{^{1}H} cross-polarization (CP)MAS NMR spectra of AlS/HfNp$_2$ (black, 1024 scans) and AlS/Hf(R)H (red, 4096 scans), at room temperature, 20kHz MAS, 100 μs contact time, 3 s recycle delay, 3.2 mm zirconia rotor, 150 MHz ^{13}C. Intensity was normalized based on number of scans for each spectrum. **C**. ^{13}C{^{1}H} FSLG-HETCOR spectrum of AlS/HfNp$_2$ 600 MHz ^{1}H, 150 MHz ^{13}C, 20 kHz MAS rate, at room temperature, 3.2 mm zirconia rotor 100 μs contact time, 3s recycle delay, internal traces shown for both dimensions. **D** ^{1}H{^{27}Al} RESPDOR AlS/Hf(R)H spectral dephasing curve for the Hf-H signal at δ ^{1}H 19.2 ppm, 400 MHz ^{1}H, 104 MHz ^{27}Al, recoupling steps of 160 μs, 3s recycle delay, 12.5 kHz MAS, 100 K, 100 μs saturation pulse on ^{27}Al at 200 W **E**. ^{1}H{^{27}Al} RESPDOR AlS/Hf(R)H dephasing curve for the signal at δ ^{1}H 0.8 ppm. 600 MHz ^{1}H, 156 MHz ^{27}Al, recoupling steps of 100 μs, 3s recycle delay, 40 kHz MAS, 298 K, 1.6 mm zirconia rotor. **F**. ^{13}C{^{27}Al} RESPDOR dephasing curve for AlS/HfNp$_2$ 400 MHz ^{1}H, 104 MHz ^{27}Al, recoupling steps of 200 μs, 3s recycle delay, 100K, 3.2 mm sapphire rotor. A contact time of 125 μs for ^{1}H-^{13}C CP was used. Dephasing curves were fit with the INTERFACES program. Dotted lines represent error range of fit dephasing curve with a 90% confidence interval.

resonance (RESPDOR)[48] was used to measure the dipolar coupling between ^{27}Al nuclei comprising the surface and ^{1}H and ^{13}C nuclei. Because the dipolar coupling strength for a given set of nuclei is directly related to distance ($\propto 1/r^3$),

internuclear distances may be extracted from this measurement. Thus, $^{1}H\{^{27}Al\}$ RESPDOR was used to estimate a H···Al distance for the Hf-H proton of AlS/Hf(R)H, yielding 4.4 ± 0.7 Å (**Figure 2D**). This result compares favorably with the DFT-computed average (inverse cube weighted average of nearest 3 Al atoms; *vide infra*) distance of 4.1 Å. A shorter H···Al distance of 3.7 ± 0.4 Å is found for AlS/Zr(R)H, also agreeing well with the DFT average of 3.9 Å (**Figure S2A**). The $^{1}H\{^{27}Al\}$ RESPDOR dephasing curve for the alkyl signal at δ_{1H} 0.8 ppm yields a distance of 5.1 ± 0.3 Å, which agrees extremely well with the DFT-derived average H···Al distance of 5.2 Å (**Figure 2E**; *vide infra*). Analogously for AlS/Zr(R)H, the signal at δ_{1H} 0.9 ppm yields a RESPDOR distance of 4.9 ± 0.5 Å, comparing favorably with the DFT average of 5.3 Å (**Figure S2B**). $^{13}C\{^{27}Al\}$ RESPDOR was also utilized to strengthen the assignments made in the ^{13}C CPMAS NMR spectrum. The signal at δ_{13C} 26.3 ppm exhibits an extremely steep dephasing curve, indicating strong dipolar coupling between the ^{13}C nuclei responsible for the signal and surface ^{27}Al nuclei. These data yield an Al-C distance of 1.9 ± 0.1 Å, implying that the carbon is bound directly to Al (**Figure 2F**), again agreeing very well with the DFT computed bond distance of 2.0 Å (*vide infra*). These data are strongly suggestive of a Hf alkyl-hydride species. Further evidence for the existence of such a species is provided by the similar AlS/Zr(R)H *via* back-to-back homonuclear single quantum - double quantum correlation spectroscopy using back-to-back (BABA) pulse scheme.[49] Here, a correlation between the Zr-H and the Zr-alkyl protons are observed, lending further credence to the presence of metal alkyl-hydrides (**Figure S3**). In-depth SSNMR characterization was not carried out for AlS/TiNp$_2$ due to its lack of thermal stability.

Catalyst Characterization - EXAFS

The combination of EXAFS and DFT computation provides additional information about the chemical and electronic structure of AlS/HfNp$_2$ (Table 1). The Hf L_{111} Edge EXAFS (Figure 3B) results indicate that AlS/HfNp$_2$ is an oxide-bound HfNp$_2$ cationic fragment with three Hf-O bonds (average distance of ~2.10 Å) and two longer Hf-C bonds (average length of ~2.29 Å; Table 1). The DFT-derived model (vide *infra*) for AlS/HfNp$_2$ shows three Hf-O bonds with lengths of 2.09-2.18 Å, which is in good agreement with the EXAFS data. In situ monitoring the EXAFS of AlS/HfNp$_2$ under hydrogenolysis conditions over a 298 – 523 K temperature range reveals gradual conversion to AlS/Hf(Np)H, with a decrease in the number of Hf-C bonds from 2.0 to 1.0, and a slight contraction of the average Hf-O bond length to ~2.09 Å (Figure S4). This is consistent with the less encumbered hydride ligand replacing a bulky Np ligand. Further H_2 treatment at 250 °C has minimal effects indicating that AlS/Hf(Np)H is stable under the present, hence catalytic conditions. The DFT analysis (see more below) shows that the three Hf-O bonds in AlS/Hf(R)H are slightly contracted to 2.06-2.20 Å vs those in AlS/HfNp$_2$, in agreement with the EXAFS data. From XANES, the Hf L_{111} edge energy increases upon forming the hydride complex compared to the dineopentyl complex for both Hf and Zr. This is consistent with the loss of an electron-donating branched alkyl group during hydride formation. Also, the XANES Zr K-edge energies for AlS/ZrNp$_2$ (18.005 keV) and AlS/Zr(R)H (18.008 keV) lie in the range of cationic complexes vs. neutrally charged *t*-Bu$_2$PhOZr(benzyl)$_3$ (17.998 keV) and Zr(benzyl)$_4$ (17.999 keV).[27, 28]

Table 1. Experimental XANES, EXAFS, and DFT-computed metrical data for supported organo-zirconium and hafnium catalysts.

Catalyst	Edge Energy (KeV)	Bond Type	N	Average Bond Length (Å)	
				EXAFS	DFT
AlS/HfNp$_2$	9.558	Hf-O	3	2.10(2)	2.10
		Hf-C	2	2.29(2)	2.17
AlS/HfRH	9.560	Hf-O	3	2.08(2)	2.12
		Hf-C	1	2.28(2)	2.16
AlS/ZrNp$_2$[a]	18.005	Zr-O	3	2.26(2)	2.21
		Zr-C	2	2.42(3)	2.17
AlS/ZrRH[a]	18.008	Zr-O	3	2.19(3)	2.15
		Zr-C	2	2.38(3)	2.20

*Mason et al. ref. [27, 28]

Catalyst Characterization - DRIFTS

The DRIFTS spectrum (**Figure 3C**) of AlS/HfNp$_2$ contains intense $\nu_{C\text{-}H}$ stretching modes in the characteristic 3000-2800 cm^{-1} region, also seen in the AlS/ZrNp$_2$ spectrum.[27, 28] This signal decreases significantly and a new signal is observed at 1940 cm^{-1} upon treatment with H_2 at 150 °C/2.5 atm for 30 min, assigned to the $\nu_{Al\text{-}H}$ stretching mode. The reduction of the $\nu_{C\text{-}H}$ modes supports a Hf-neopentyl$_2$ → AlS/Hf(alkyl)H conversion scenario.

Catalytic Reactivity Characterization

Scope of AlS/MNp$_2$-mediated polyolefin hydrogenolysis

Previously, we reported that AlS/ZrNp$_2$ is a highly effective precatalyst for pristine polyethylene homopolymer and α-olefin-ethylene copolymer hydrogenolysis under mild conditions of temperature and H_2 pressure.[27, 28] In this study, we extend the scope to preconsumer commercially relevant polyolefins with and without standard additives and use more industrially relevant reaction methodology. In the previous study, hydrogenolysis by AlS/ZrNp$_2$ was performed in an optically transparent 350 mL glass reactor heated by an oil bath. The reactants were stirred by a standard magnetic stir bar at 300 rpm. This setup was effective for the hydrogenolysis of liquid hydrocarbons such as hexadecane and low-viscosity lab-synthesized polyolefins. Using the glass reactor afforded excellent activities for the least viscous preconsumer 1-octene-ethylene copolymer sourced from The Dow Chemical Company, PECO1 (melt index = 1000 g · (10 min)$^{-1}$), providing a hydrogenolysis activity of 5350 (mol CH_2 units) · (mol Zr)$^{-1}$ · (h)$^{-1}$ (**Table 2, Entry**

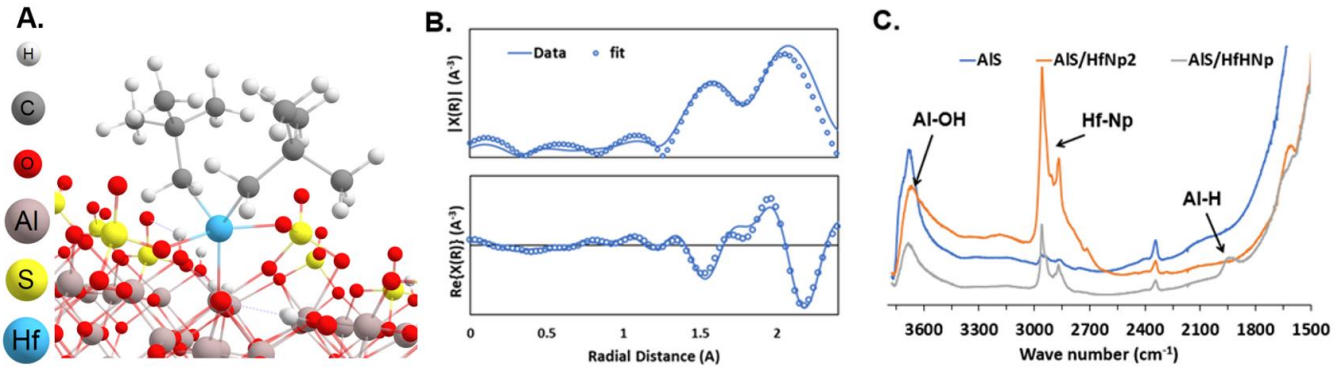

Figure 3. **A**. DFT-derived AlS/HfNp$_2$ structure. **B**. EXAFS pRDFs and fits of AlS/HfNp$_2$ at the Hf L_{111} edge. **C**. DRIFTS spectra of AlS support, AlS/HfNp$_2$, and AlS/Hf(R)H.

1). The more viscous PECO2 (melt index = 30 g · (10 min)$^{-1}$).and PECO3 (melt index = 3 g · (10 min)$^{-1}$) undergo significantly diminished hydrogenolysis activities of 3320 and 772 (mol CH_2 units) · (mol Zr)$^{-1}$ · (h)$^{-1}$, respectively (**Table 2, Entries 2 & 3**), likely reflecting stirring hindered by the greater viscosity.

The issue of this mass transport/H_2 starvation effect in the glass reactors was addressed by using a 25 mL Parr autoclave reactor with a PTFE liner and magnetically coupled stirring, which was anticipated to address the stirring limitations of the glass reactor for more viscous polymers. A stirring rate of 1500 rpm was found to be optimal, with activity plateauing at higher rates (**Figure S6**). For the autoclave reactions, the polyolefin hydrogenolysis products were analyzed as follows: At the end of the reaction, stirring is ceased, and the reactor is cooled to 25 °C via forced-air cooling. The reactor is vented, with headspace samples being collected if needed, then opened. The stirring attachment and PTFE liner containing the liquid and solid products are removed and weighed. The solids and liquids are washed from the liner and vacuum filtered through a filter paper using dichloromethane as the solvent (DCM). DCM insoluble solids collected on the filter paper are dried and weighed, with the mass corrected for the amount of catalyst used. Mass unaccounted for by the solids and liquids are assumed to be volatiles released during venting. Further analysis of the products can be performed via high-temperature GPC for the solids, GC/MS for the liquids, and GC/FID for volatiles (**Figures S7-S12**). The combined mass of the volatile and DCM-soluble product fractions as a percentage of the initial polyolefin mass is used to estimate the percent conversion reported. This may be a slight underestimate of actual polymer conversion, as the solid fractions produced in the autoclave are waxes with a somewhat lower molecular mass than the starting polymer. Although the autoclave H_2 pressure was increased to compensate for the smaller reactor volume, this is not expected to greatly affect the rate based on previous kinetic measurements.[27, 28] In summary, the Parr reactor is found to provide a roughly 10-fold increase in activity for all polyolefin substrates (**Table 2, Entries 4- 6**).

Comparative Activity/Thermal Stability Trends

Catalytic polyolefin hydrogenolysis experiments with AlS/TiNp$_2$, AlS/ZrNp$_2$, and AlS/HfNp$_2$ were performed over a temperature range to determine the relative hydrogenolysis activities. The polymer used initially was the 1-octene-ethylene copolymer PECO1, which has the highest melt flow index of the analyzed polymers, to ensure that higher temperatures did not result in greater activity simply due to more extensive viscosity reduction/ease of mixing. All catalysts are active for hydrogenolysis at 150 ^{0}C, under which conditions the activity trend is Zr >> Hf > Ti (**Table 3, Entries 1, 3,** and **5**). All three catalysts produce high ratios of liquid : volatile products at 150 ^{0}C. The Zr and Hf catalysts

Table 2. PE hydrogenolysis data for glass and stainless steel autoclave reactors with AlS/ZrNp$_2$-derived catalysts[a]

Entry	Polymer Sample	PE Melt Flow Index[b]	Reactor Type	Reaction Time (min)	Catalyst loading (Zr mol %)	Product Distribution (solid%, liquid%, volatile%)			Activity[c]
1	PECO1	1000	Glass	15	0.063	14.8,	67.7,	17.5	5350
2	PECO2	30	Glass	25	0.064	9.7,	8.6,	81.7	3320
3	PECO3	3	Glass	120	0.054	8.2,	25.1,	66.7	772
4	PECO1	1000	Parr	20	0.006	24.0,	57.2,	18.8	35500
5	PECO2	30	Parr	20	0.006	22.6,	66.3,	11.1	36300
6	PECO3	3	Parr	60	0.012	1.4,	48.5,	50.1	7930

[a]Reaction conditions: 200 ^{0}C, 1.0 g polyethylene (Glass reactor, 300 rpm), (Parr reactor, PECO1&2, 1900 rpm; PECO3, 400 rpm). [b]Units in g · (10 min)$^{-1}$. [c]Activity units in (mol CH_2 units) · (mol Zr)$^{-1}$ · (h)$^{-1}$

Table 3. Temperature-dependent polyolefin hydrogenolysis data for AlS/MNp_2-derived catalysts[a]

Entry	Catalyst Metal Center	Temperature (°C)	Reaction Time (min)	Catalyst loading (M mol %)	Product Distribution (solid%, liquid%, volatile%)	Activity[b]
1	Ti	150	120	0.012	37.6, 52.7, 9.6	2450
2	Ti	200	120	0.012	52.6, 40.1, 7.2	1900
3	Zr	150	40	0.006	10.1, 74.5, 15.4	21600
4	Zr	200	20	0.006	24.0, 57.2, 18.8	35500
5	Hf	150	60	0.012	9.1, 72.6, 18.2	7000
6	Hf	200	30	0.012	12.5, 76.4, 11.1	13500

[a]Reaction conditions: neat substrate, 1.0 g PECO1 polymer, Parr reactor, 17 atm H_2, 1500 rpm [b]Activity units: (mol CH_2 equiv. of volatiles + liquids) · $(mol\ M)^{-1}$ · $(h)^{-1}$

both afford over 70% conversion by mass to liquid hydrocarbons. On raising the reaction temperature to 200 ^{0}C, the activity of the Zr and Hf catalysts continues to increase (**Table 3, Entries 4 & 6**) while the activity of the Ti catalyst falls (**Table 3, Entry 2**), suggesting deactivation due to thermal degradation. Liquid product selectivity falls for the Zr catalyst at 200 ^{0}C but remains >70% for the Hf catalyst. For both the Zr and Hf catalysts, the hydrogenolysis activity declines on increasing temperature from 200 to 250 ^{0}C, suggesting thermal degradation begins in this range. Therefore, the relative AlS/MNp_2-derived catalyst thermal stability trend under the present PE hydrogenolysis conditions is approximately Hf ≈ Zr > Ti. This trend follows the approximate thermal stability trend reported for the corresponding less stable MNp_4 precursors.[50] Furthermore, pristine $TiNp_4$ is known to reach 50% decomposition in 13 h at 60 °C, whereas the supported ogano-Ti catalyst may be stored at room temperature for over a month with no significant decrease in catalytic activity. That the AlS/MNp_2 complexes exhibit greater thermal stability than their MNp_4 precursors is not uncommon for SSHCs[23-26], and presumably reflects both immobilization/binding to the surface and cationic charge which may impede thermolytic intramolecular C-H activation processes.

Polyolefin microstructure and additive effects on AlS/MNp_2-mediated hydrogenolysis

The commercially available consumer 1-octene-ethylene copolymer (PECO) samples used in the present catalytic hydrogenolysis experiments varied in molecular mass and comonomer content, and some also contained varying amounts of proprietary additive packages, which typically include antioxidants, plasticizers, and flame retardants, among other substances.[51] A commercial isotactic polypropylene (*i*-PP) was also surveyed. Under identical hydrogenolysis reaction conditions, the different polymer types afford distinct product distributions, as shown in **Table 4**. AlS/$HfNp_2$ is capable of efficient hydrogenolysis of post-consumer polyethylene homopolymers and α-olefin copolymers, such as bottle caps (**Table 4, Entry 1**) and a HDPE milk jug (**Table 4, Entry 3**), although the rates are somewhat lower than that of other polymers despite higher reaction temperatures, partially due to the molten jug sample clinging to the reactor stirring shaft. HDPE milk jug results were improved by altering the stirring rate to 300 rpm for the first 25% of the reaction time, followed by 1000 rpm for the remainder. This catalyst is also competent for mediating the hydrogenolysis of isotactic polypropylene (**Table 4, Entry 5**), although at a somewhat lower rate than the pre-consumer PECOs, possibly reflecting steric hindrance about the C-C bond.

AlS/$ZrNp_2$ is also competent to hydrogenolyze the post-consumer α-olefin copolymers (bottle caps and HDPE milk jug) and isotactic polypropylene (**Table 4, Entries 2, 4,** and **6**). The PE bottle cap hydrogenolysis activity is lower for the Zr catalyst than the Hf catalyst. *i*-PP and HDPE milk jug activities are approximately twice that of the Hf catalyst, in contrast to the preconsumer 1-octene-ethylene copolymer PECO1 for which the AlS/$ZrNp_2$-catalyzed activity was approximately 170% greater than that of the Hf catalyst (**Table 3, Entries 3-6**). This may reflect persisting mass transfer issues for the highly viscous post-consumer polymers or differences in resistance to additive effects.

Regarding possible inhibitory effects of polyolefin additives on the hydrogenolysis, experiments were performed with a PECO2 α-olefin copolymer having the additives first removed via an accepted sonication/extraction protocol.[52] Note that the catalytic results for AlS/$HfNp_2$ are indistinguishable from those with an as-received PECO2 additive-containing sample, indicating that the present additives have at most a minor effect on the catalytic process under these conditions (**Table 4, Entries 7 & 8**). Conversely, the PECO2 sample with additives removed was mildly more active for hydrogenolysis by the AlS/$ZrNp_2$ catalyst (**Table 4, Entries 9 & 10**). Though AlS/$ZrNp_2$ is capable of full conversion of the additive containing α-olefin copolymer with low catalyst loadings and mild conditions, these results suggest inhibition by the additives for this catalyst. The hydrogenolysis of other additive containing PECO samples by AlS/$HfNp_2$ show similar activities but distinct product ratios (**Table 4, Entries 11, 12**, and **13**) which presumably reflect differences in polyolefin molecular masses and comonomer content.

Some post-consumer polyolefins having high melt viscosities, especially high-density polyethylene (HDPE) sourced from a commercial milk jug, proved to be especially challenging, despite the enhanced stirring offered by the Parr reactor. The diminished hydrogenolysis rates likely

Table 4. Catalytic polyolefin hydrogenolysis data over AlS/MNp_2 as a function of polymer type[a]

Entry	Catalyst Metal Center	Polymer Sample	Temperature (°C)	Reaction Time (min)	Catalyst loading (M mol %)	Product Distribution (solid%, liquid%, volatile%)			Activity[b]
1	Hf	PE Bottle Cap	200	60	0.012	26.5,	17.3,	56.2,	5340
2	Zr	PE Bottle Cap	200	30	0.006	85.7,	3.6,	10.7,	4460
3	Hf	HDPE Milk Jug[f]	200	120	0.036	7.3,	0,	92.7,	1210
4	Zr	HDPE Milk Jug[f]	200	60	0.018	66.7,	0,	33.3,	2120
5	Hf	*i*-PP	200	60	0.012	25.5,	59.7,	14.7,	5560
6	Zr	*i*-PP	200	30	0.006	68.0,	24.3,	7.7,	10200
7	Hf	PECO2	150	60	0.012	3.2,	64.2,	32.6,	7500
8	Hf	PECO2[c]	150	60	0.012	2.9,	68.0,	29.1,	7530
9	Zr	PECO2	150	40	0.006	16.1,	69.1,	14.8,	19700
10	Zr	PECO2[c]	150	40	0.006	1.3,	65.5,	33.2,	22900
11	Hf	PECO1	150	60	0.012	9.1,	72.6,	18.2,	7000
12	Hf	PECO4[d]	150	60	0.012	1.1,	62.4,	36.5,	7600
13	Hf	PECO5[e]	150	60	0.012	2.0,	48.0,	40.0,	7580

[a]General reaction conditions: neat substrate, 25mL Parr reactor, 17 ATM H_2, 1500 rpm. [b]Activity units: (mol CH_2 equiv. of volatiles + liquids) · (mol Hf)$^{-1}$ · (h)$^{-1}$.[c] Additive-free PECO2. [d] Melt index = 3. [e] Melt index = 5. [f]HDPE milk jug reaction conditions: neat substrate, 25mL Parr reactor, 17 ATM H_2, 300 rpm for first 25% of reaction time, 1000 rpm for remainder.

reflect poor contact and mass transport between catalyst and viscous polymer. To address this issue, a solvent was added to the reaction mixture to moderate the overall melt viscosity by promoting polymer chain disentanglement, allowing better contact with the catalyst.[53]

Dry decalin was employed as the reaction solvent as it was found to be surprisingly inert towards hydrogenolysis over AlS/$ZrNp_2$. Addition of small quantities of decalin enhance the activity by up to 2.5-fold and improve liquid selectivity, which is slightly underestimated due to solvent condensation in the reactor head (see SI). Addition of 0.25 g decalin/g HDPE gave the highest activity of 3298 (mol CH_2 units) · (mol Zr)$^{-1}$ · (h)$^{-1}$ (**Figure 4**). Notably, the products of reactions involving decalin included liquid hydrocarbons, which were not observed after HDPE milk jug reactions under neat reaction conditions (**Table 4, Entries 3 & 4**). Hydrogenolysis rates slow at high decalin contents, possibly reflecting polymer dilution and/or competitive inhibition.

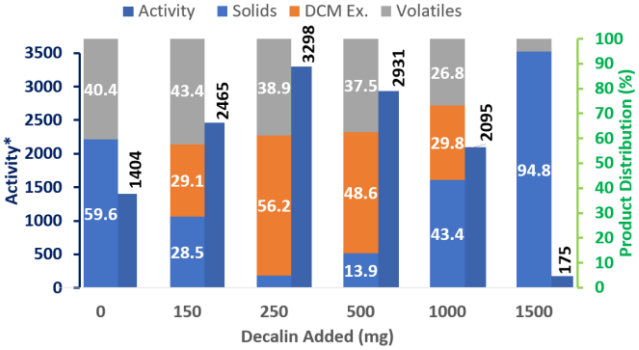

Figure 4. Solvent-assisted HDPE hydrogenolysis. Conditions: 1.0 g HDPE, 0.09 g Zr cat. (0.018% mol Zr loading) 200 °C / 17 atm H_2 / 90 min / 25 mL Parr Reactor / 1500 rpm. Activity units: (mol CH_2 equiv. of volatiles + liquids) · (mol Hf)$^{-1}$ · (h)$^{-1}$.

Discussion

The present group IV AlS/MNp_2 catalysts were prepared by chemisorbing the corresponding MNp_4 precursors onto AlS, which had been partially dehydroxylated at 550 ˚C under flowing O_2. Low temperature ^{1}H MAS NMR spectra of AlS/$HfNp_2$ reveal signals at δ_{1H} 2.9 and 1.1 ppm (**Figure 2A**), much like those of the ^{1}H MAS NMR spectrum of AlS/$ZrNp_2$.[27, 28] Additionally, $^{13}C\{^1H\}$ CP-MAS NMR reveals both Hf-CH_2- and Al-CH_2- signals, like that seen for the Zr analogue (**Figure 2B**). While chemisorption *via* Hf-C bond protonolysis is a potential pathway for formation of AlS/$HfNp_2$ (**Figure 5A**), the presence of Al-CH_2- signals suggests that there is an additional pathway.

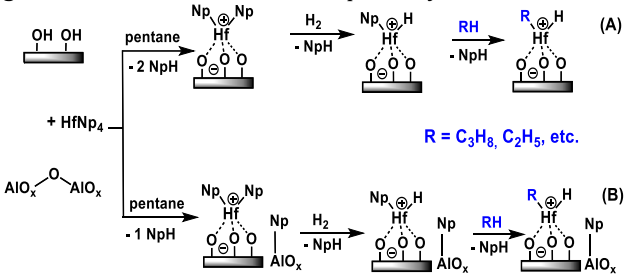

Figure 5. Plausible pathways for $HfNp_4$ chemisorption and hydrogenolysis. **A**. Hf-C protolyis and Hf-C hydrogenolysis. **B.** Hf-C protolyis, Np transfer to the surface, and Hf-C hydrogenolysis.

Alkide transfer has been proposed in the past for the chemisorption of similar organo-group IV species on sulfated metal oxides.[54, 55] In this case, a neopentyl ligand would be protonolyzed from $HfNp_4$ to produce a $HfNp_3$ species which would then further react with surface functionalities (e.g., undergo the aforementioned alkide transfer) produce a $HfNp_2^+$ species (**Figure 5B**). The large decrease in the Hf-CH_2- signal intensity in the $^{13}C\{^1H\}$ CP-MAS NMR of AlS/$HfNp_2$ after H_2 treatment suggests that if both species

are present in similar quantities; they likely have very similar, if not identical reactivity (**Figures 5A** and **5B**).

After treating AlS/HfNp$_2$ with H$_2$ to form AlS/Hf(R)H, a new signal at δ_{1H} 19.2 ppm in the low temperature ^{1}H MAS NMR spectrum becomes visible (**Figure 2A**). The concomitant decrease in the alkyl C-H resonances at δ_{1H} 1.1 ppm suggests that a Hf-H is responsible for this new signal. This is supported by the EXAFS data, with the apparent coordination number dropping from 5 to 4 (**Figure 3B**; **Table 1**), suggesting replacement of one ligand with a hydride. The change in Hf K-edge energy follows the same trend as the Zr analogue before and after H$_2$ treatment.[21] Specifically, the increase in K-edge energy after H$_2$ treatment implies a lower electron density about the metal, which agrees well with the proposed Hf alkyl-hydride structure. The alkyl R is likely a remaining neopentyl group in the precatalyst, which is rapidly hydrogenolyzed upon the addition of heat and excess hydrogen. Note that the ^{13}C{^{1}H} FSLG-HETCOR NMR spectrum (**Figure 2C**), as well as the ^{1}H{^{27}Al} RESPDOR and ^{13}C{^{27}Al} RESPDOR NMR structural and geometrical data are in good accord with those derived from EXAFS and DFT computation (vide infra).

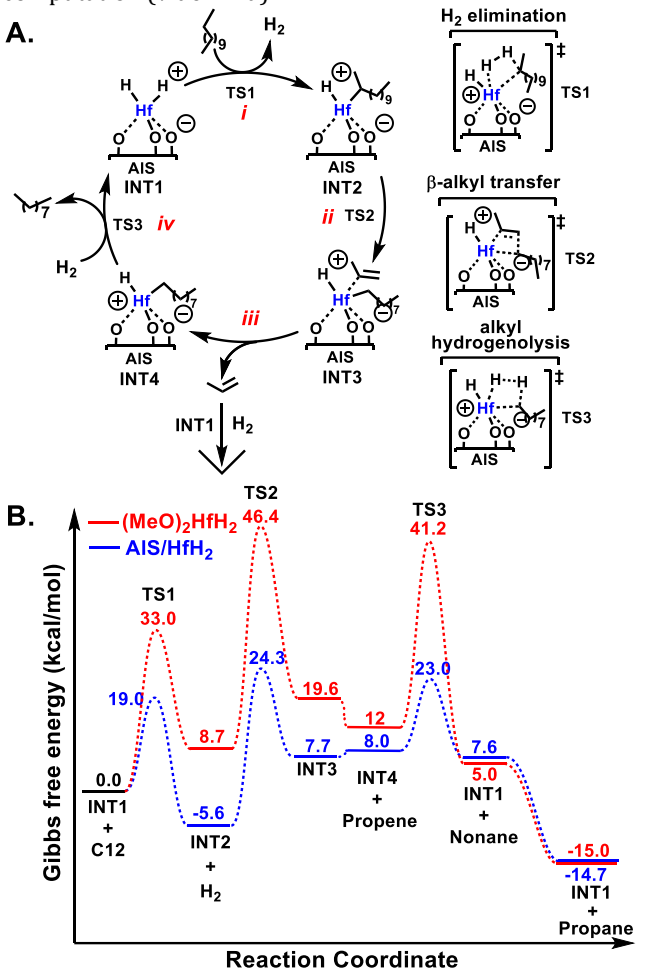

Figure 6. A. Plausible mechanism for polyolefin hydrogenolysis catalyzed by AlS/HfH$_2$. **B.** Comparative computed energy profiles for cation-like AlS/HfH$_2$ (blue) vs neutrally charged (MeO)$_2$HfH$_2$ (red) -catalyzed n-dodecane hydrogenolysis.

In order to gain deeper insight into the reaction mechanism of polyolefin hydrogenolysis, with a particular focus on the role of the group IV metal center and acidic support/ligand effects, the energy profile was computed using *n*-dodecane as a model substrate (**Figure 6**). Thus, in the first step, the supported hafnium hydride (AlS/HfH$_2$; **INT1**) reacts with the polyolefin (*n*-dodecane) via a concerted four-membered cyclic transition state (**TS1**), during which an H$_2$ molecule is eliminated, and a Hf-alkyl bond is formed yielding **INT2** (**Figure 6A**, step *i*). This step has a 19.2 kcal/mol barrier (**TS1**) and is exergonic by -5.6 kcal/mol (**Figure 6B**). Note that the analogous step for the formally neutral (MeO)$_2$HfH$_2$ catalyst is endergonic by 8.7 kcal/mol and has a barrier of 33.0 kcal/mol, significantly greater than the corresponding AlS/HfH$_2$ catalyst (**Figure 6B**). Next, similarly to previously proposed mechanisms involving an AlS/Zr metal center,[27, 28] a β-alkyl transfer step can occur, yielding **INT3**, which still has an olefin (propene) coordinated to the Hf center (**Figure 6A**, step *ii*). This step is endergonic by 13.3 kcal/mol, has a barrier of 29.9 kcal/mol (**TS2**), and is the rate-determining β-alkyl transfer step of the catalytic process (**Figure 6B**). The presence of the coordinated olefin in **INT3** explains why, in most of the polyolefin hydrogenolysis products, a slight incorporation of branching is observed by NMR since, in principle, the Hf-alkyl fragment in **INT3** can undergo olefin reinsertion. Note that the energetic barrier (**TS2**) in the cationic Hf complex is lower by 16.5 kcal/mol compared to the formally neutral (MeO)$_2$HfH$_2$ catalyst (**Figure 6B**), highlighting once more the importance of the super acidic support/ligand in the catalysis. Next, the olefin can dissociate from the metal center yielding **INT4** (**Figure 6A**, step *iii*), which can then undergo a slightly exergonic (-0.4 kcal/mol) alkyl hydrogenolysis step to regenerate catalyst **INT 1** and produce a shorter alkane (nonane) (**Figure 6A**, step iv). This step has a barrier of 15 kcal/mol (**TS3**) and is once again significantly lower versus the formally neutrally charged Hf catalyst (**Figure 6B**). Finally, the previously produced olefin (propene) is hydrogenated to propane in a strongly exergonic step (-22.3 kcal/mol), making the overall process energetically favorable (**Figure 6B**). Note that the overall computed energetic span of the supported cationic AlS/HfNp$_2$- derived catalyst is higher by 3.8 kcal/mol than that of the analogous AlS/ZrNp$_2$-derived catalyst, in good agreement with the observed slightly slower reaction rates.

Catalytic hydrogenolysis activity and selectivity trends

The trend in polyolefin hydrogenolysis activity is overall Zr > Hf > Ti. The activity differences between the Zr and Hf catalysts are consistent with the respective energy barriers of the DFT computed mechanism. The barrier of the rate-determining β-alkyl transfer step is computed to be 29.9 kcal/mol for AlS/HfNp$_2$ and 26.1 kcal/mol for AlS/ZrNp$_2$ (**Figure 6B**).[27, 28] AlS/ZrNp$_2$, AlS/TiNp$_2$, and AlS/HfNp$_2$ are capable of hydrogenolyzing additive-containing PECO, and the additive present in the tested samples appears to have little effect on the activity for AlS/ZrNp$_2$ and no effect for AlS/HfNp$_2$. Both AlS/ZrNp$_2$ and AlS/HfNp$_2$ are capable of high liquid hydrocarbon product selectivity, up to 74.5% at 150 °C for AlS/ZrNp$_2$ and 76.4% at 200 °C for AlS/HfNp$_2$. The product distribution is dependent on temperature, reaction time, and the substrate. The substrate effect on selectivity can be explained by the variable level of branching in the copolymer samples tested.

Post-consumer polyolefin bottle caps and milk jugs can be rapidly hydrogenolyzed by the present catalysts under solventless conditions, although rates are significantly

slower than the pre-consumer polymers, an effect seen more strongly for the AlS/$ZrNp_2$ than the AlS/$HfNp_2$. This lower activity is partially due to the extremely high viscosity of these samples, which cling to the reactor stirring shaft resulting in poor contact with the catalyst. Beginning the reaction with a slower stirring rate allows more rapid hydrogenolysis of these resistant polyolefins **(Figure 4; Table 4, Entry 4)**. The addition of small amounts of decalin as a solvent, which is surprisingly inert to these catalysts, results in a more significant increase to the hydrogenolysis rate for postconsumer HDPE.

The approximate catalyst thermal stability trend scales as Hf ≈ Zr > Ti, with the Hf and Zr catalysts showing similar decreases in activity when increasing reaction temperatures from 200 to 250 ^{0}C. The increased stability of the catalyst compared to the molecular precursors can be attributed to the stabilizing effect of the support.

Conclusions

Two new electrophilic group IV complexes, AlS/$TiNp_2$ and AlS/$HfNp_2$, were prepared by chemisorption of the corresponding MNp_4 precursor onto highly Brønsted acidic sulfated alumina and are compared to the previously prepared AlS/$ZrNp_2$ congener. The structure of the Hf catalyst, supported by EXAFS, XANES, ICP, DRIFTS and SSNMR measurements, is in good agreement with the DFT-derived structure and is structurally/reactivity-wise similar to, not identical to, the AlS/$ZrNp_2$ analogue. Such loosely coordinated cationic d^0 species undergo facile catalytic β-alkyl elimination which, when coupled with rapid four-center Hf-C/H-C/H-H σ-bond metathesis processes effect rapid hydrogenolysis of diverse polyolefins. In autoclave reactions with efficient stirring, the AlS/$ZrNp_2$-derived catalyst provides up to 10-fold greater polyethylene hydrogenolysis rates versus reactions in a glass reactor using a magnetic stir bar. These catalysts are capable of efficient hydrogenolysis of a variety of pre- and post- consumer plastics in the presence of standard additives, which have no significant effect on the reaction for AlS/$HfNp_2$ and only a mild effect for AlS/$ZrNp_2$. While most pre- and post- consumer plastics can be hydrogenolyzed under neat conditions, the addition of decalin as a solvent can alter the product distribution and significantly enhance the reactivity of challenging substrates such as HDPE milk jugs. The relative activity trend is approximately Zr >> Hf > Ti, which is consistent with the relative DFT computed energy barriers. The AlS/MNp_2 thermal stability trend is Hf ≈ Zr > Ti, which is consistent with the approximate thermal stability of the MNp_4 precursors.[50] The energy span DFT analysis implicates β-alkyl elimination as the turnover-limiting C-C scission step which is particularly facile in these cationic d^0 complexes, but not so in the formally neutrally charged analogues.

Experimental

All procedures for air- and moisture-sensitive compounds were carried out with rigorous exclusion of O_2 and moisture in flame- or oven-dried Schlenk-type glassware interfaced to a high-vacuum (10^{-5} –10^{-6} Torr) line or in an argon-filled M-Braun glovebox with a high capacity recirculator (<1 ppm O_2). Argon used on high-vacuum lines (Airgas, UHP-grade) was purified by passage through MnO/vermiculite and activated Davidson 4 Å molecular sieve columns. All solvents were dispensed from activated alumina/CuO columns prior to use. n-pentane (Sigma) was further purified by drying over Na/K alloy followed by passage through a fiberglass filter in an argon glovebox. Aluminum oxide was purchased from Nanostructured and Amorphous Materials (gamma, nanopowder 20–30 nm). Sulfuric acid (98%) was purchased from Fisher. Oxygen (UHP grade) used for calcination was purchased from Airgas and used without further purification. Deuterium (Sigma) and hydrogen (Airgas, UHP) were purified by passage through an oxygen/ moisture trap (Matheson, model MTRP-0042-XX). Zirconium(IV) chloride, hafnium(IV) chloride, titanium(IV) chloride, and neopentylmagnesium chloride (1.0 M solution in Et_2O) were purchased from Sigma and used without further purification. Tetrakis(neopentyl)zirconium, tetrakis(neopentyl)hafnium, and tetrakis(neopentyl)titanium (MNp_4) were synthesized according to a modification of a literature procedure.[50] In a typical synthesis, neopentylmagnesium chloride (4.4 mmol) was added dropwise to a suspension of MCl_4 (1.0 mmol) in ether at −78 °C. The mixture was allowed to stir for 2h, slowly warmed to room temperature, then stirred for an additional 2h at room temperature. The solvent was removed in vacuo, and the resulting solids were extracted with pentane. The pentane filtrate was isolated, and the solvent was removed in vacuo to yield colorless solids. The crude products were purified by sublimation at 70 °C and ~10^{-6} Torr. All MNp_4 products were colorless microcrystalline solids. Polymers were placed under high vacuum for 18h before use in the hydrogenolysis reactions.

Physical and analytical measurements

Inductively coupled plasma (ICP) analysis was performed by Galbraith Laboratories Inc., Knoxville, TN, USA. Diffuse reflectance infrared spectroscopy (DRIFTS) measurements were taken under Ar on a Thermo 6700 infrared spectrometer equipped with a Harrick Praying Mantis DRIFTS attachment. ZnSe windows were used for the DRIFTS cell. Anhydrous KBr with an Ar glovebox atmosphere in the cell was used as a background.

NMR Spectroscopy

Solid state NMR measurements were obtained at DOE Ames National Laboratory with either a Bruker Avance III system equipped with a 1.6 mm or 3.2 mm probe (600 MHz ^{1}H), or a Bruker Avance III system equipped with a low-temperature 3.2 mm DNP probe (400 MHz ^{1}H). A 3s recycle delay was used for all experiments unless otherwise stated. ^{1}H (600 MHz) MAS Hahn-echo experiments performed at room temperature utilized a 1.6 mm probe with 40 kHz MAS with a 90° excitation pulse on ^{1}H at 100 kHz radiofrequency (RF) power. An echo delay of 4 rotor periods (100 μs) was used to minimize probe background signal. ^{13}C{^{1}H} CP-MAS (600 MHz ^{1}H, 150 MHz ^{13}C) spectra were taken at room temperature with a 3.2 mm Varian triple resonance probe with 100 μs contact time and 100 kHz RF power on ^{1}H and a 20 kHz MAS rate. CP-MAS experiments were optimized on a sample-by sample basis to satisfy the Hartmann-Hahn condition during CP. ^{1}H{^{27}Al} RESPDOR (600 MHz ^{1}H, 156 MHz ^{27}Al) experiments were taken at room temperature on a Varian 1.6 mm probe at 40 kHz MAS with a 90° excitation pulse on ^{1}H at 100kHz RF and $SR4_1^2$ recoupling with recoupling steps of 100 μs. A saturation pulse of 30μs at 60W was applied on ^{27}Al. ^{1}H (400 MHz) MAS Hahn-Echo experiments performed at 100K utilized a 3.2 mm Bruker DNP probe at 12.5 kHz

MAS, a 90° excitation pulse at 100kHz RF with an 80 μs echo delay. Variable-temperature ^{1}H NMR experiments utilized the same parameters. ^{13}C{^{27}Al} RESPDOR (100 MHz ^{13}C, 104 MHz ^{27}Al) was performed at 100K on a 3.2 mm Bruker DNP probe at 10 kHz MAS with ^{13}C{^{1}H} CP used to excite ^{13}C and SFAM recoupling with recoupling steps of 200 μs. A 75 μs saturation pulse was applied on the ^{27}Al channel at 200W. A REDOR box was utilized so that the X-channel could serve to excite both ^{27}Al and ^{13}C (from www.nmr-service.de).

X-ray absorption spectroscopy

X-ray absorption near edge structure (XANES) and extended X-ray absorption fine structure (EXAFS) measurements at Zr K-edge (17,998 eV) and Hf L_{III} -edge were performed at the 5 BM-D beamline of the DND-CAT at the Advanced Photon Source. A double Si (111) monochromator was used for energy selection with an energy resolution of $\Delta E/E = 1.4 \times 10^{-4}$. The X-ray energy was calibrated using metallic reference foils. The incident X-ray intensity was measured by a spectroscopy-grade ionization chamber (FMB-Oxford) filled with 600 He/100 N_2 (Torr) and was detuned to 60% of its maximum for harmonic rejection. EXAFS spectra were collected in fluorescence mode using a passivated implanted planar silicon (PIPS) detector (Canberra). The sample and the detector were positioned 45° and 90°, respectively, to the X-ray beam direction. Energy scans were executed from 250 eV below to 550 eV above the absorption edges, which produces the EXAFS spectra. The catalysts, AlS/ZrNp_2 (1.4 wt% Zr) and AlS/HfNp_2 (3.28 wt% Hf), were pressed into sample holders for the EXAFS measurements. The samples were sealed airtight in a THMS600 Linkam cell inside the glove box, which was pressed with ultrapure Ar gas. Positive Ar pressure was maintained throughout the measurement. After measuring the AlS/HfNp_2 sample, in-situ catalyst hydrogenolysis was carried out by flowing H_2 gas with a flow rate of 50 sccm at room temperature with EXAFS data collected every 15 min for 2 h until no further changes were observed. This was followed by heating the sample to 150 °C with continued H_2 flow. Data were collected every 15 min for up to 2 h. finally, the sample for further heated to 250 °C for 2 hours. No changes were observed after this step of the treatment. There was a change in the structure during the hydrogenolysis reaction at room temperature and at elevated temperatures of 150 °C and 250 °C. Additionally, an ex situ sample was prepared by heating the sample to 150 °C for 30 min under 2.5 atm H_2 pressure in a glass reactor to test the functioning of the in-situ setup. XANES data extraction, normalization, and background subtraction was performed using Demeter:Athena. EXAFS data analysis was carried out using the software Demeter:Artemis. The bond lengths (R) and coordination number (N) were obtained by a least-square fit in the R-space of the nearest neighbors using k_2-weighted Fourier transform fitting parameter.

Computational details

DFT-based simulations were performed with the/Quickstep package, using a hybrid Gaussian and plane wave method. A double-quality DZVP Gaussian basis set was employed for the Al and Hf atoms, and a triple-quality TZVP Gaussian basis set was employed for all the other atoms. The Goedecker–Teter–Hutter pseudopotentials46 and a 400 Ry plane wave cutoff were used to expand the densities obtained with the Perdew–Burke–Ernzerhof (PBE) exchange-correlation density functional, and vdW forces are taken into account with the Grimme D3 Method. Only the gamma point was considered in a supercell approach. Periodic boundary conditions are applied in all directions of space. Molecular graphics were produced by the CHEMCRAFT graphical package. Enthalpic and entropic contributions along the reaction pathway were evaluated by performing the frequency calculation of the molecular species at 298.15 K and 1 atm as implemented in the ORCA software. In this context, adsorbed catalysts were modeled by simple molecular species, and only the entropic contribution related to vibrational motion is considered. ORCA calculations were performed at the level of the B3LYP-D3/ZORA-def2-TZVP (for C and H atoms) and SARC-ZORA-TZVP (for Hf). The enthalpic and entropic contributions were then "appended" to the SCF energy profile to obtain the Gibbs free energy profile.

ASSOCIATED CONTENT

Supporting Information. Experimental procedures; GPC traces; DFT calculations; EXAFS, atomic coordinates from DFT computation. This material is available free of charge via the Internet at http://pubs.acs.org

AUTHOR INFORMATION

Corresponding Author

* Takeshi Kobayashi - U.S. DOE Ames Laboratory, Ames, Iowa 50011-3020, United States; https://orcid.org/0000-0002-6366-0925; Email: takeshi@iastate.edu

* Yosi Kratish – Department of Chemistry and the Materials Research Center, Northwestern University, Evanston, Illinois 60208, United States; orcid.org/0000-0001-5279-0268; Email: yosi.kratish@northwestern.edu

*Tobin J. Marks – Department of Chemistry and the Materials Research Center, Northwestern University, Evanston, Illinois 60208, United States; orcid.org/0000-0001-8771-0141; Email: t-marks@northwestern.edu

Notes

The authors declare no competing financial interest.

Acknowledgements

Financial support was provided by the U.S. Department of Energy, Office of Science, Office of Basic Energy Sciences under Award Number DOE DE-FG02-03ER15457 to the Institute for Catalysis in Energy Processes (ICEP) at Northwestern University (NU) and The Dow Chemical Company. This work made use of IMSERC facilities at NU, which have received support from Soft and Hybrid Nanotechnology Experimental (SHyNE) Resource (NSF ECCS-2025633), Int. Institute of Nanotechnology (IIN), and NU. This work made use of the NU QBIC supported by NASA Ames Research Center Grant NNA04CC36G. This work made use of the REACT Facility of NU's Center for Catalysis and Surface Science supported by a grant from the DOE (DE-SC0001329). This work used the DuPont-Northwestern-Dow Collaborative Access Team (DND-CAT) 5BM-D beamline at the Advanced Photon Source (APS). DND-CAT is supported by NU, E. I. DuPont de Nemours & Co., and The Dow Chemical Company. APS is supported by DOE at Argonne National Laboratory under Contract No. DE-AC02-06CH11357. This research was supported in part by the computational resources and staff contributions provided by the Quest High Performance Computing Facility at NU, which is jointly supported by the Office of the Provost, the Office for Research, and NU Information

Technology. A part of this work (solid-state NMR) was supported by the U.S. Department of Energy (DOE), Office of Science, Basic Energy Sciences, Chemical Sciences, Geosciences, and Biosciences Division. The research was performed at the Ames National Laboratory, which is operated for the U.S. DOE by Iowa State University under contract # DE-AC02-07CH11358. A.H.M. thanks the U.S. Department of Energy, Office of Science, Office of Basic Energy Sciences for a SCGSR Graduate Fellowship tenured at Ames National Laboratory. The SCGSR program is administered by the Oak Ridge Institute for Science and Education for the DOE under contract number DE - SC0014664.

References

(1) Geyer, R.; Jambeck, J. R.; Law, K. L. Production, use, and fate of all plastics ever made. *Science Advances* **2017**, *3* (7), e1700782. DOI: 10.1126/sciadv.1700782.

(2) Ragaert, K.; Delva, L.; Van Geem, K. Mechanical and chemical recycling of solid plastic waste. *Waste Manag* **2017**, *69*, 24-58. DOI: 10.1016/j.wasman.2017.07.044.

(3) Hong, M.; Chen, E. Y. X. Chemically recyclable polymers: a circular economy approach to sustainability. *Green Chemistry* **2017**, *19* (16), 3692-3706. DOI: 10.1039/C7GC01496A.

(4) Chaudhari, U. S.; Johnson, A. T.; Reck, B. K.; Handler, R. M.; Thompson, V. S.; Hartley, D. S.; Young, W.; Watkins, D.; Shonnard, D. Material Flow Analysis and Life Cycle Assessment of Polyethylene Terephthalate and Polyolefin Plastics Supply Chains in the United States. *ACS Sustainable Chemistry & Engineering* **2022**, *10* (39), 13145-13155. DOI: 10.1021/acssuschemeng.2c04004.

(5) Eriksson, O.; Finnveden, G. Plastic waste as a fuel - CO_2-neutral or not? *Energy & Environmental Science* **2009**, *2* (9), 907-914. DOI: 10.1039/B908135F.

(6) Anuar Sharuddin, S. D.; Abnisa, F.; Wan Daud, W. M. A.; Aroua, M. K. A review on pyrolysis of plastic wastes. *Energy Conversion and Management* **2016**, *115*, 308-326. DOI: 10.1016/j.enconman.2016.02.037.

(7) Zhou, X.-L.; He, P.-J.; Peng, W.; Lü, F.; Shao, L.-M.; Zhang, H. From plastics to methane and carbon spheres: The evolution of pyrolysis products during pyrolysis under autogenic atmosphere. *Journal of Analytical and Applied Pyrolysis* **2022**, *161*, 105421. DOI: 10.1016/j.jaap.2021.105421.

(8) Rahimi, A.; García, J. M. Chemical recycling of waste plastics for new materials production. *Nature Reviews Chemistry* **2017**, *1* (6), 0046. DOI: 10.1038/s41570-017-0046.

(9) Chu, M.; Tu, W.; Yang, S.; Zhang, C.; Li, Q.; Zhang, Q.; Chen, J. Sustainable chemical upcycling of waste polyolefins by heterogeneous catalysis. *SusMat* **2022**, *2* (2), 161-185. DOI: 10.1002/sus2.55.

(10) Kots, P. A.; Vance, B. C.; Vlachos, D. G. Polyolefin plastic waste hydroconversion to fuels, lubricants, and waxes: a comparative study. *Reaction Chemistry & Engineering* **2022**, *7* (1), 41-54. DOI: 10.1039/D1RE00447F.

(11) Sánchez-Rivera, K. L.; Huber, G. W. Catalytic Hydrogenolysis of Polyolefins into Alkanes. *ACS Central Science* **2021**, *7* (1), 17-19. DOI: 10.1021/acscentsci.0c01637.

(12) Zhang, F.; Zeng, M.; Yappert, R. D.; Sun, J.; Lee, Y.-H.; LaPointe, A. M.; Peters, B.; Abu-Omar, M. M.; Scott, S. L. Polyethylene upcycling to long-chain alkylaromatics by tandem hydrogenolysis/aromatization. *Science* **2020**, *370* (6515), 437-441. DOI: 10.1126/science.abc5441.

(13) Rorrer, J. E.; Beckham, G. T.; Román-Leshkov, Y. Conversion of Polyolefin Waste to Liquid Alkanes with Ru-Based Catalysts under Mild Conditions. *JACS Au* **2021**, *1* (1), 8-12. DOI: 10.1021/jacsau.0c00041.

(14) Celik, G.; Kennedy, R. M.; Hackler, R. A.; Ferrandon, M.; Tennakoon, A.; Patnaik, S.; LaPointe, A. M.; Ammal, S. C.; Heyden, A.; Perras, F. A.; et al. Upcycling Single-Use Polyethylene into High-Quality Liquid Products. *ACS Central Science* **2019**, *5* (11), 1795-1803. DOI: 10.1021/acscentsci.9b00722.

(15) Rorrer, J. E.; Ebrahim, A. M.; Questell-Santiago, Y.; Zhu, J.; Troyano-Valls, C.; Asundi, A. S.; Brenner, A. E.; Bare, S. R.; Tassone, C. J.; Beckham, G. T.; et al. Role of Bifunctional Ru/Acid Catalysts in the Selective Hydrocracking of Polyethylene and Polypropylene Waste to Liquid Hydrocarbons. *ACS Catalysis* **2022**, *12* (22), 13969-13979. DOI: 10.1021/acscatal.2c03596.

(16) Chu, M.; Wang, X.; Wang, X.; Lou, X.; Zhang, C.; Cao, M.; Wang, L.; Li, Y.; Liu, S.; Sham, T.-K.; et al. Site-Selective Polyolefin Hydrogenolysis on Atomic Ru for Methanation Suppression and Liquid Fuel Production. *Research* **2023**, *6*, 0032. DOI: 10.34133/research.0032.

(17) Conk, R. J.; Hanna, S.; Shi, J. X.; Yang, J.; Ciccia, N. R.; Qi, L.; Bloomer, B. J.; Heuvel, S.; Wills, T.; Su, J.; et al. Catalytic deconstruction of waste polyethylene with ethylene to form propylene. *Science* **2022**, *377* (6614), 1561-1566. DOI: 10.1126/science.add1088.

(18) Goldman, A. S.; Roy, A. H.; Huang, Z.; Ahuja, R.; Schinski, W.; Brookhart, M. Catalytic Alkane Metathesis by Tandem Alkane Dehydrogenation-Olefin Metathesis. *Science* **2006**, *312* (5771), 257-261. DOI: 10.1126/science.1123787.

(19) Tennakoon, A.; Wu, X.; Paterson, A. L.; Patnaik, S.; Pei, Y.; LaPointe, A. M.; Ammal, S. C.; Hackler, R. A.; Heyden, A.; Slowing, I. I.; et al. Catalytic upcycling of high-density polyethylene via a processive mechanism. *Nature Catalysis* **2020**, *3* (11), 893-901. DOI: 10.1038/s41929-020-00519-4.

(20) Zhang, F.; Zeng, M.; Yappert, R. D.; Sun, J.; Lee, Y. H.; LaPointe, A. M.; Peters, B.; Abu-Omar, M. M.; Scott, S. L. Polyethylene upcycling to long-chain alkylaromatics by tandem hydrogenolysis/aromatization. *Science* **2020**, *370* (6515), 437-441. DOI: 10.1126/science.abc5441.

(21) Zichittella, G.; Ebrahim, A. M.; Zhu, J.; Brenner, A. E.; Drake, G.; Beckham, G. T.; Bare, S. R.; Rorrer, J. E.; Román-Leshkov, Y. Hydrogenolysis of Polyethylene and Polypropylene into Propane over Cobalt-Based Catalysts. *JACS Au* **2022**, *2* (10), 2259-2268. DOI: 10.1021/jacsau.2c00402 From NLM.

(22) Vance, B. C.; Kots, P. A.; Wang, C.; Granite, J. E.; Vlachos, D. G. Ni/SiO_2 catalysts for polyolefin deconstruction via the divergent hydrogenolysis mechanism. *Applied Catalysis B: Environmental* **2023**, *322*, 122138. DOI: 10.1016/j.apcatb.2022.122138.

(23) Pelletier, J. D. A.; Basset, J.-M. Catalysis by Design: Well-Defined Single-Site Heterogeneous Catalysts. *Accounts of Chemical Research* **2016**, *49* (4), 664-677. DOI: 10.1021/acs.accounts.5b00518.

(24) Liu, Y.; Agarwal, A.; Kratish, Y.; Marks, T. J. Single-Site Carbon-Supported Metal-Oxo Complexes in Heterogeneous Catalysis: Structure, Reactivity, and Mechanism. *Angewandte Chemie International Edition* **2023**, (Article ASAP), e202304221. DOI: 10.1002/anie.202304221.

(25) Korzyński, M. D.; Copéret, C. Single sites in heterogeneous catalysts: separating myth from reality. *Trends in Chemistry* **2021**, *3* (10), 850-862. DOI: 10.1016/j.trechm.2021.07.003.

(26) Copéret, C.; Comas-Vives, A.; Conley, M. P.; Estes, D. P.; Fedorov, A.; Mougel, V.; Nagae, H.; Núñez-Zarur, F.; Zhizhko, P. A. Surface Organometallic and Coordination Chemistry toward Single-Site Heterogeneous Catalysts: Strategies, Methods, Structures, and Activities. *Chemical Reviews* **2016**, *116* (2), 323-421. DOI: 10.1021/acs.chemrev.5b00373.

(27) Mason, A. H.; Motta, A.; Das, A.; Ma, Q.; Bedzyk, M. J.; Kratish, Y.; Marks, T. J. Rapid atom-efficient polyolefin plastics hydrogenolysis mediated by a well-defined single-site electrophilic/cationic organo-zirconium catalyst. *Nature Communications* **2022**, *13* (1), 7187. DOI: 10.1038/s41467-022-34707-6.

(28) Mason, A. H.; Motta, A.; Das, A.; Ma, Q.; Bedzyk, M. J.; Kratish, Y.; Marks, T. J. Facile Polyolefin Plastics Hydrogenolysis Catalyzed by a Surface Electrophilic d^0 Hydride *ChemRxiv* preprint **2021**, DOI: 10.26434/chemrxiv-2021-7bx90.

(29) Dufaud, V.; Basset, J. M. Catalytic Hydrogenolysis at Low Temperature and Pressure of Polyethylene and Polypropylene to

Diesels or Lower Alkanes by a Zirconium Hydride Supported on Silica-Alumina: A Step Toward Polyolefin Degradation by the Microscopic Reverse of Ziegler-Natta Polymerization. *Angew Chem Int Ed Engl* **1998**, *37* (6), 806-810. DOI: 10.1002/(sici)1521-3773(19980403)37:6<806::Aid-anie806>3.0.Co;2-6.

(30) Williams, L. A.; Guo, N.; Motta, A.; Delferro, M.; Fragalà, I. L.; Miller, J. T.; Marks, T. J. Surface structural-chemical characterization of a single-site d^0 heterogeneous arene hydrogenation catalyst having 100% active sites. *Proceedings of the National Academy of Sciences* **2013**, *110* (2), 413-418. DOI: 10.1073/pnas.1220240110.

(31) Gu, W.; Stalzer, M. M.; Nicholas, C. P.; Bhattacharyya, A.; Motta, A.; Gallagher, J. R.; Zhang, G.; Miller, J. T.; Kobayashi, T.; Pruski, M.; et al. Benzene Selectivity in Competitive Arene Hydrogenation: Effects of Single-Site Catalyst···Acidic Oxide Surface Binding Geometry. *Journal of the American Chemical Society* **2015**, *137* (21), 6770-6780. DOI: 10.1021/jacs.5b03254.

(32) Stalzer, M. M.; Delferro, M.; Marks, T. J. Supported Single-Site Organometallic Catalysts for the Synthesis of High-Performance Polyolefins. *Catalysis Letters* **2015**, *145* (1), 3-14. DOI: 10.1007/s10562-014-1427-x.

(33) Gao, J.; Zhu, L.; Conley, M. P. Cationic Tantalum Hydrides Catalyze Hydrogenolysis and Alkane Metathesis Reactions of Paraffins and Polyethylene. *Journal of the American Chemical Society* **2023**, *145* (9), 4964-4968. DOI: 10.1021/jacs.2c13610.

(34) Witzke, R. J.; Chapovetsky, A.; Conley, M. P.; Kaphan, D. M.; Delferro, M. Nontraditional Catalyst Supports in Surface Organometallic Chemistry. *ACS Catalysis* **2020**, *10* (20), 11822-11840. DOI: 10.1021/acscatal.0c03350.

(35) Corma, A.; García, H. Lewis Acids: From Conventional Homogeneous to Green Homogeneous and Heterogeneous Catalysis. *Chemical Reviews* **2003**, *103* (11), 4307-4366. DOI: 10.1021/cr030680z.

(36) O'Reilly, M. E.; Dutta, S.; Veige, A. S. β-Alkyl Elimination: Fundamental Principles and Some Applications. *Chemical Reviews* **2016**, *116* (14), 8105-8145. DOI: 10.1021/acs.chemrev.6b00054.

(37) Yang, X.; Jia, L.; Marks, T. J. Carbon-carbon activation at electrophilic d_0 centers. Facile, regioselective β-alkyl shift-based ring-opening polymerization reactions of methylenecyclobutane. *Journal of the American Chemical Society* **1993**, *115* (8), 3392-3393. DOI: 10.1021/ja00061a073.

(38) Arata, K.; Hino, M. Solid catalyst treated with anion: XVIII. Benzoylation of toluene with benzoyl chloride and benzoic anhydride catalysed by solid superacid of sulfate-supported alumina. *Applied Catalysis* **1990**, *59* (1), 197-204. DOI: 10.1016/S0166-9834(00)82197-1.

(39) Berkson, Z. J.; Björgvinsdóttir, S.; Yakimov, A.; Gioffrè, D.; Korzyński, M. D.; Barnes, A. B.; Copéret, C. Solid-State NMR Spectra of Protons and Quadrupolar Nuclei at 28.2 T: Resolving Signatures of Surface Sites with Fast Magic Angle Spinning. *JACS Au* **2022**, *2* (11), 2460-2465. DOI: 10.1021/jacsau.2c00510.

(40) Zhao, Z.; Xiao, D.; Chen, K.; Wang, R.; Liang, L.; Liu, Z.; Hung, I.; Gan, Z.; Hou, G. Nature of Five-Coordinated Al in γ-Al_2O_3 Revealed by Ultra-High-Field Solid-State NMR. *ACS Central Science* **2022**, *8* (6), 795-803. DOI: 10.1021/acscentsci.1c01497.

(41) Tosin, G.; Santini, C. C.; Taoufik, M.; Mallmann, A. D.; Basset, J.-M. Reactivity of Tetraneopentylhafnium, $Hf(CH_2tBu)_4$, with Silica Surfaces. *Organometallics* **2006**, *25* (14), 3324-3335. DOI: 10.1021/om060178f.

(42) Abraham, A.; Prins, R.; van Bokhoven, J. A.; van Eck, E. R. H.; Kentgens, A. P. M. Multinuclear Solid-State High-Resolution and ^{13}C-{^{27}Al} Double-Resonance Magic-Angle Spinning NMR Studies on Aluminum Alkoxides. *The Journal of Physical Chemistry B* **2006**, *110* (13), 6553-6560. DOI: 10.1021/jp055058k.

(43) Lee, M.; Goldburg, W. I. Nuclear-Magnetic-Resonance Line Narrowing by a Rotating rf Field. *Physical Review* **1965**, *140* (4A), A1261-A1271. DOI: 10.1103/PhysRev.140.A1261.

(44) van Rossum, B. J.; Förster, H.; de Groot, H. J. M. High-Field and High-Speed CP-MAS13C NMR Heteronuclear Dipolar-Correlation Spectroscopy of Solids with Frequency-Switched Lee–Goldburg Homonuclear Decoupling. *Journal of Magnetic Resonance* **1997**, *124* (2), 516-519. DOI: 10.1006/jmre.1996.1089.

(45) Schnierle, M.; Klostermann, S.; Kaya, E.; Li, Z.; Dittmann, D.; Rieg, C.; Estes, D. P.; Kästner, J.; Ringenberg, M. R.; Dyballa, M. How Solid Surfaces Control Stability and Interactions of Supported Cationic Cu^{I}(dppf) Complexes — A Solid-State NMR Study. *Inorganic Chemistry* **2023**, *62* (19), 7283-7295. DOI: 10.1021/acs.inorgchem.3c00351.

(46) Boyle, T. J.; Reuel, P. C.; Wiemann, D. K.; Settecerri, T.; Omana, M. A.; Cramer, R. E. Structurally characterized aluminum alkoxide derivatives for aerosol spray materials production. *Polyhedron* **2022**, *223*, 115958. DOI: 10.1016/j.poly.2022.115958.

(47) Werghi, B.; Bendjeriou-Sedjerari, A.; Sofack-Kreutzer, J.; Jedidi, A.; Abou-Hamad, E.; Cavallo, L.; Basset, J.-M. Well-defined silica supported aluminum hydride: another step towards the utopian single site dream? *Chemical Science* **2015**, *6* (10), 5456-5465. DOI: 10.1039/C5SC02276B.

(48) Perras, F. A.; Kanbur, U.; Paterson, A. L.; Chatterjee, P.; Slowing, II; Sadow, A. D. Determining the Three-Dimensional Structures of Silica-Supported Metal Complexes from the Ground Up. *Inorg Chem* **2022**, *61* (2), 1067-1078. DOI: 10.1021/acs.inorgchem.1c03200.

(49) Saalwächter, K.; Lange, F.; Matyjaszewski, K.; Huang, C.-F.; Graf, R. BaBa-xy16: Robust and broadband homonuclear DQ recoupling for applications in rigid and soft solids up to the highest MAS frequencies. *Journal of Magnetic Resonance* **2011**, *212* (1), 204-215. DOI: 10.1016/j.jmr.2011.07.001.

(50) Davidson, P. J.; Lappert, M. F.; Pearce, R. Silylmethyl and related complexes II. Preparation, spectra, and thermolysis of the tetraneopentyls of titanium, zirconium, and hafnium. *Journal of Organometallic Chemistry* **1973**, *57* (2), 269-277. DOI: 10.1016/S0022-328X(00)86607-3.

(51) Zweifel, H.; Maier, R. D.; Schiller, M.; Amos, S. E. *Plastics additives handbook*; Hanser Gardner Publications, 2001.

(52) Nielson, R. C. Extraction and Quantitation of Polyolefin Additives. *Journal of Liquid Chromatography* **1991**, *14* (3), 503-519. DOI: 10.1080/01483919108049266.

(53) Miller-Chou, B. A.; Koenig, J. L. A review of polymer dissolution. *Progress in Polymer Science* **2003**, *28* (8), 1223-1270. DOI: 10.1016/S0079-6700(03)00045-5.

(54) Zhang, J.; Mason, A. H.; Wang, Y.; Motta, A.; Kobayashi, T.; Pruski, M.; Gao, Y.; Marks, T. J. Beyond the Active Site. Cp*$ZrMe_3$/Sulfated Alumina-Catalyzed Olefin Polymerization Tacticity via Catalyst···Surface Ion-Pairing. *ChemCatChem* **2021**, *13* (11), 2564-2569. DOI: 10.1002/cctc.202100406.

(55) Zhang, J.; Mason, A. H.; Motta, A.; Cesar, L. G.; Kratish, Y.; Lohr, T. L.; Miller, J. T.; Gao, Y.; Marks, T. J. Surface vs Homogeneous Organo-Hafnium Catalyst Ion-Pairing and Ligand Effects on Ethylene Homo- and Copolymerizations. *ACS Catalysis* **2021**, *11* (6), 3239-3250. DOI: 10.1021/acscatal.0c04678.

TOC Graphic